

pubs.acs.org/NanoLett Letter

Bioinspired Ruthenium—Porphyrin Electrocatalysts with Atomic N_4/N_2 Proximal Sites for Efficient Proton-Coupled Electron Transfer in Water Electrolysis

Zhenyang Zhao, Chao He, Luchang Liu, Yijuan Zheng, Wenhui Xiang, Qinlong Wen, Yinghan Wang, Evgeniya Sheremet, Tian Ma,* and Shuang Li*



Cite This: Nano Lett. 2025, 25, 8310-8319



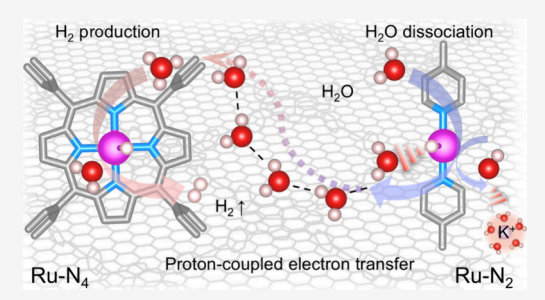
ACCESS I

III Metrics & More

Article Recommendations

Supporting Information

ABSTRACT: Mimicking the proton-coupled electron transfer (PCET) pathways of natural enzymes, we engineer a porphyrin-based ruthenium coordination polymer (Ru-PCPN) with precisely positioned atomic-level N_4/N_2 proximal sites through molecular-scale coordination engineering. This bioinspired architecture establishes a dual-site relay mechanism where the Ru- N_2 center accelerates water dissociation kinetics while the adjacent Ru- N_4 site optimizes hydrogen recombination. Experimental and theoretical results reveal that the sub-nanometer-proximate N_4/N_2 sites function as proton donor—acceptor pairs, enabling directional proton transfer via PCET and synergistically enhancing water electrolysis. When integrated with carbon substrates, the Ru-PCPN@CB



catalyst demonstrates exceptional hydrogen evolution performance in alkaline conditions, achieving a low overpotential at 10 mA cm $^{-2}$ (42 mV, comparable to 44 mV of Pt/C), high mass activity and TOF of 9.02 A mg $^{-1}$ and 4.73 s $^{-1}$ (\sim 7.0 and 3.6 times of Pt/C), and good stability. This work establishes atomic-scale coordination proximity as a new paradigm for breaking scaling relationships in multistep electrocatalysis.

KEYWORDS: bioinspired design, porphyrin-based coordination polymer, single-atom catalysis, proton-coupled electron transfer, electrocatalysts

he quest for sustainable energy sources has propelled the development of efficient and eco-friendly methods for hydrogen production, with the hydrogen evolution reaction (HER) being a cornerstone in this endeavor. 1-3 Among various HER catalysts, Pt-based electrocatalysts are still recognized as "the Master Key" for triggering a highperformance HER due to their fast dynamics matching the moderate Pt-H bond. 4-6 Unfortunately, the activity and stability of Pt-based catalysts significantly decline in industrial alkaline media due to the sluggish water dissociation kinetics, in addition to their high cost and scarcity, which impede their large-scale application and drive people to pursue a more available alternative to Pt-based electrocatalysts.^{7,8} Ruthenium (Ru), as a promising alternative for Pt, has demonstrated encouraging catalytic activity for HER, especially in alkaline media, owning to its much better water dissociation kinetics. 9,10 Therefore, numerous efforts have been devoted to developing high-performance and low-cost Ru-based HER catalysts. 11-14

As investigated in last decades, the morphology, ^{15,16} conductivity, ^{17,18} electronic structures, ^{19,20} and coordination structures^{21–23} of Ru nanoparticles/clusters play important roles in the HER performance. ^{24,25} Among these, single-atomic Ru-based catalysts possess maximum atom utilization efficiency, and isolated active sites have become hotspots. ^{26–28}

Recently, Ru metal atomically distributed in various supporting materials has been reported to exhibit excellent HER performance.^{29–31} For instance, carbon-based substrates have been employed to stabilize the atomic-level Ru dispersion. Song et al. 32 reported a unique ternary Ru-N₄-P coordination structure fabricated via an in situ confined pyrolysis process, where monodispersed Ru atoms are supported on N, P dualdoped graphene, demonstrating enhanced performance in alkaline HER with a small overpotential of 78 mV to achieve a current density of 10 mA cm⁻². Lou et al.³³ reported a singleatom Ru-based catalyst modified with an edge-rich carbon matrix prepared via high-temperature pyrolysis, achieving a low overpotential of 83 mV at 10 mA cm⁻². Additionally, atomic Ru anchored on other substrates such as metal carbides, metal oxidates, metal-organic frameworks (MOFs), and layered double hydroxides (LDHs) has been extensively reported. 34-37 However, the atomic microenvironments of most reported Ru

Received: March 7, 2025 Revised: May 6, 2025 Accepted: May 6, 2025 Published: May 9, 2025





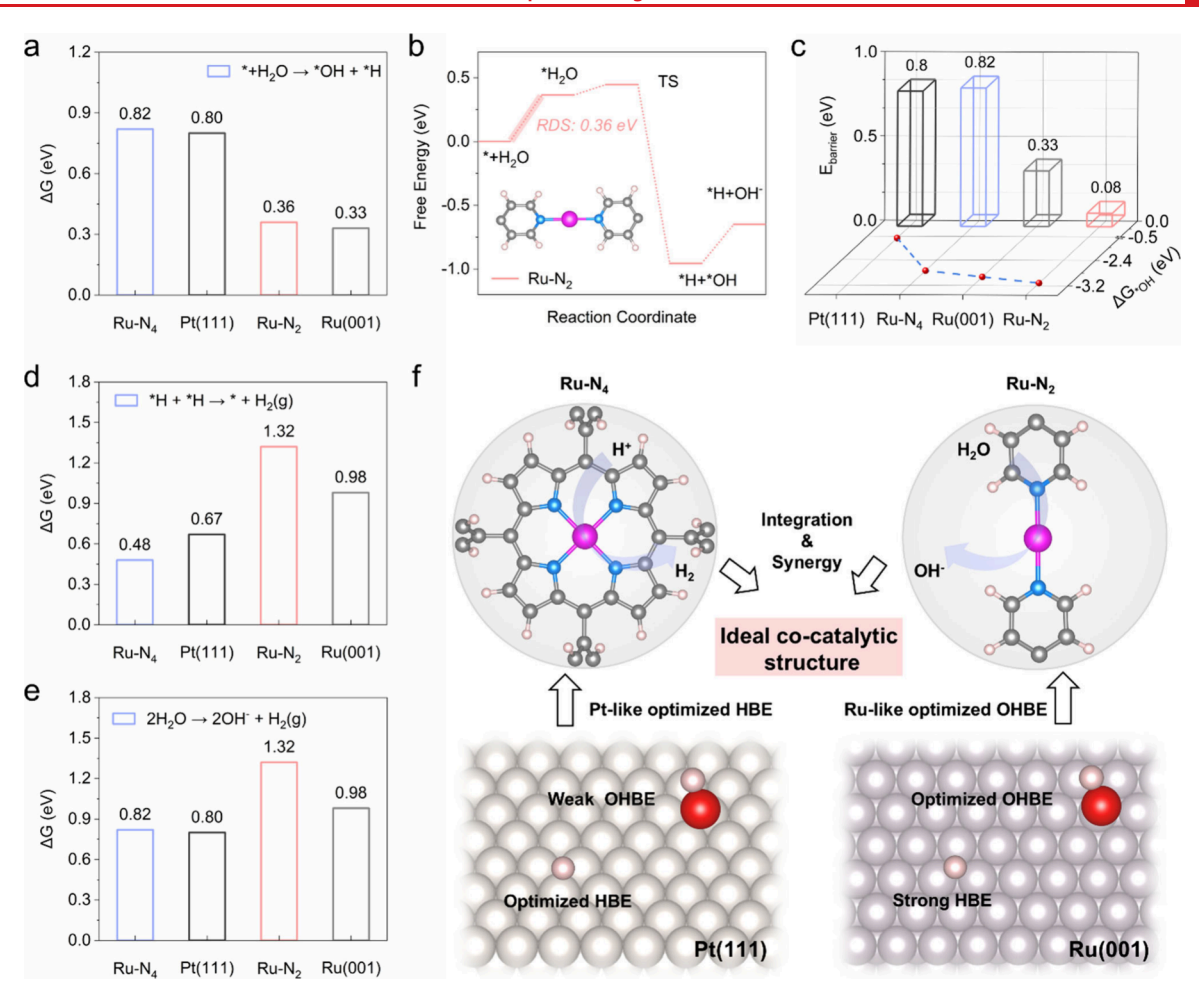


Figure 1. Theoretical analysis and comparison of the intrinsic HER activity of Ru-based catalysts. a) Rate-determining step energy barrier of water decomposition (* + $H_2O \rightarrow *OH + *H$). b) The calculated free energy diagram for water decomposition of Ru-N₂. c) The correlation between the theoretical $\Delta G_{^*OH}$ and E_{barrier} (transition state energy barrier of water decomposition). d) The rate-determining step energy barrier of hydrogen recombination (*H + *H \rightarrow * + H_2). e) Rate-determining step energy barrier of the whole alkaline HER process (2 $H_2O + 2e^- \rightarrow 2OH^- + H_2$). f) Schematic structure design strategy (OHBE, *OH binding energy; HBE, *H binding energy).

single-atom catalysts cannot be precisely controlled, which makes it difficult to investigate the exact mechanisms on different Ru sites. In this circumstance, a perfect model of Ru catalyst precisely controlled coordination environments is highly desired to further push mechanism understanding and performance enhancement.

In natural and artificial systems, the proton-coupled electron transfer (PCET) reactions are fundamental to energy transformation reactions and are ubiquitous throughout chemistry and biology.³⁸⁻⁴¹ For instance, the natural co-catalytic enzyme system of cellobiose dehydrogenase (CDH) and lytic polysaccharide monooxygenase (LPMO) can utilize electron transfer mediated by solvent water to significantly enhance the oxidative cleavage of insoluble polysaccharides. 42 Shao-Horn et al. 43 reported that the hydration shell of a cation can function as a proton donor, facilitating PCET to substantially enhance CO2-to-methanol conversion kinetics on the immobilized molecular cobalt-based catalyst. Recent studies suggest that designing enzyme-inspired catalytic microenvironments with co-catalytic sites enables precise atomic-scale regulation of local reaction environments, providing a highly controlled approach to enhance catalytic performance. 44-46 By biomimetic porphyrin structure, Peng et al. 47 reported a precise Rubased pincer complex-bridged Cu-porphyrin polymer (CuPorRu-N₃) via Schiff-base condensation that exhibited exceptional durability and a low overpotential of 114 mV at 10 mA cm⁻² in alkaline conditions, due to efficient electron transfer from Cu to Ru-N₃ catalytic sites. This bioinspired innovative cocatalytic design strategy and PCET present a promising pathway for developing efficient and selective Ru-based catalysts capable of overcoming sluggish reaction kinetics, which is extremely desirable but remains a considerable challenge.

Herein, density functional theory (DFT) calculations are combined with structural characterizations to compare the intrinsic activity of the porphyrin-based $Ru-N_4$ structure and $Ru-N_2$ structure. Our study identified that the low-coordinated $Ru-N_2$, with metallic Ru-like activity, can efficiently promote H_2O dissociation, while the higher-coordinated $Ru-N_4$ shows similar activity to metallic Pt in *H binding energy, which can effectively facilitate H recombination. Inspired by the bioinspired co-catalytic design strategy and PCET reactions in natural and artificial systems, we designed a unique porphyrin-based ruthenium coordination polymer structure (Ru-PCPN) with $Ru-N_4$ porphyrin centers connected with $Ru-N_2$ sites at the molecular level for high-performance HER catalysts in both acidic and alkaline conditions. Impressively, a synergistic effect between these

Nano Letters pubs.acs.org/NanoLett Letter

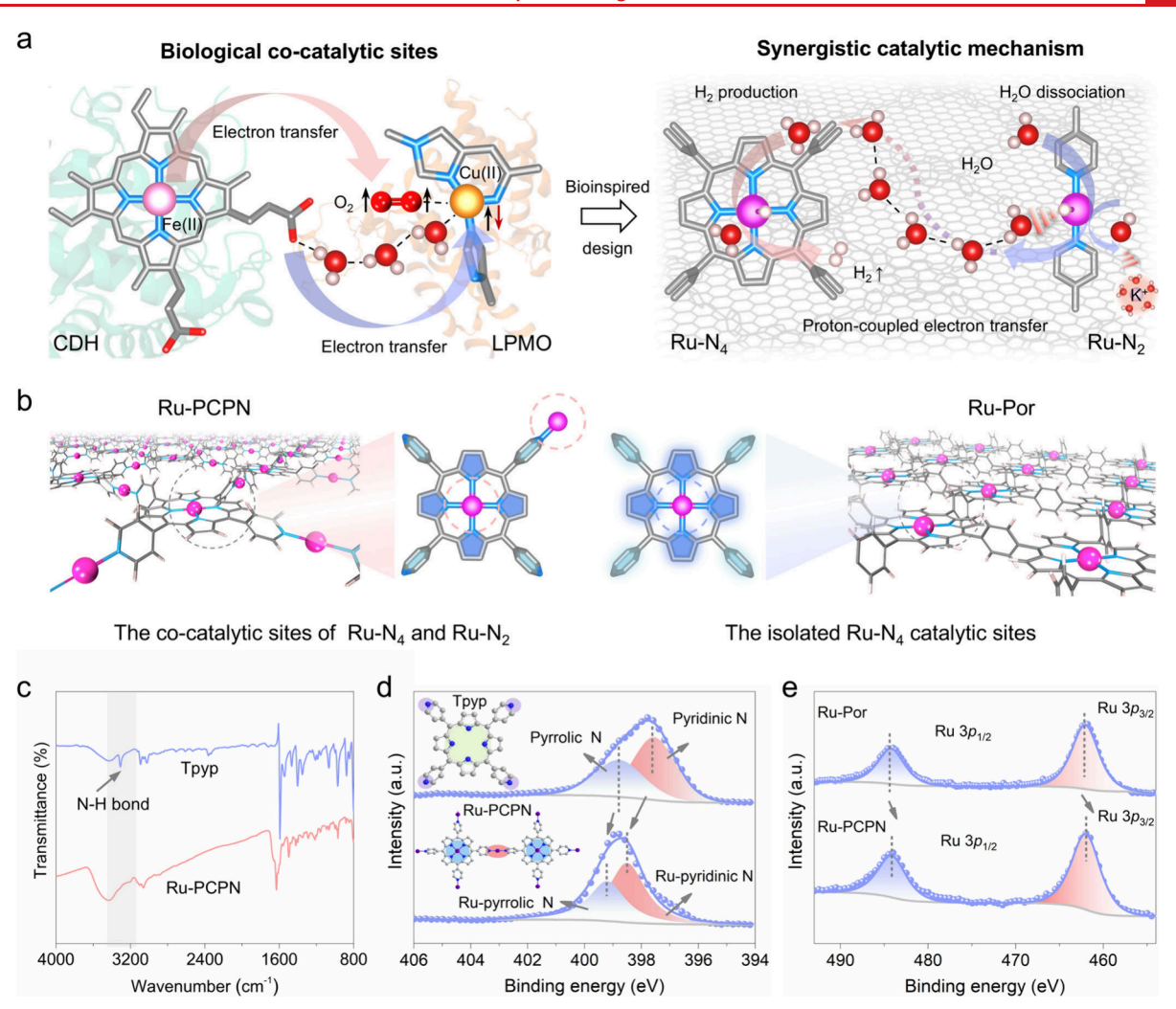


Figure 2. Design strategy and structural characterization of the Ru-PCPN electrocatalysts. a) Schematic illustration of bioinspired high/low-coordinated Ru-PCPN. b) The structure diagram of Ru-PCPN and Ru-Por electrocatalysts. c) FT-IR spectra of Tpyp ligand and Ru-PCPN. d) The N 1s XPS of Tpyp and Ru-PCPN. e) The Ru 3p XPS of Ru-PCPN and Ru-Por.

two sites happens, where the Ru–N $_2$ can transfer the H atoms generated from water dissociation to the adjacent Ru–N $_4$ site through PCET and therefore achieve a rapid H $_2$ release and excellent intrinsic activity for alkaline HER. When the Ru-PCPN was assembled on conductive carbon black via $\pi-\pi$ stacking interaction, the resulting Ru-PCPN@CB exhibited great catalytic activity for HER in 1 M KOH solution with a lower overpotential (42 mV, compared with 44 mV of Pt/C) at 10 mA cm $^{-2}$ and a higher mass activity and TOF value of 9.02 A mg $^{-1}$ and 4.73 s $^{-1}$ (~7.0 and 3.6 times those of Pt/C). This study provides essential insights into the crucial roles of precise coordination sites and catalytic microenvironments in HER catalysis.

First, DFT calculation was employed to systematically investigate the water dissociation behavior of Ru-based catalysts with different coordination states, such as highly coordinated Ru–N₄, low-coordinated Ru–N₂, and metallic Ru(001), along with the comparison to metallic Pt(111). As depicted in Figure 1a,b and Figure S1, the energy barriers for the rate-determining step (RDS) of water dissociation (* + $\rm H_2O \rightarrow *OH + *H)$ for Ru–N₄ are as high as 0.82 eV, similar to Pt(111) (0.80 eV). In contrast, Ru–N₂ exhibits a much lower energy barrier (0.36 eV), akin to Ru(001) (0.30 eV), indicating that Ru–N₂ has an excellent water dissociation

ability like Ru(001). There is a positive correlation between the water dissociation transition state energy barrier (E_{barrier}) $*H_2O \rightarrow *OH + *H$, the usual RDS step) and the free energy of OH capture (ΔG_{*OH} , * + OH \rightarrow *OH), especially for catalysts with the same active centers, which can provide a reference for qualitatively assessing the water dissociation capabilities of materials (Figure 1c and Figure S2). Considering that the complete alkaline HER process should also include the hydrogen recombination step (*H + *H \rightarrow * + H_2), the corresponding energy barriers were calculated for Ru-N₄, Ru-N₂, Ru(001), and Pt(111), yielding 0.48, 1.32, 0.98, and 0.67 eV, respectively (Figure 1d and Figure S3). Notably, $Ru-N_4$, with its unique planar structure (Figure S4), demonstrates superior hydrogen recombination capabilities, with a barrier of 0.48 eV, comparable to that of Pt(111) and superior to those of Ru-N₂ and Ru(001). It is noteworthy that Ru-N₂ exhibits water dissociation promotion capabilities comparable to Ru(001), while Ru-N₄ demonstrates hydrogen recombination efficiency similar to that of Pt(111) (Figure 1e,f). Based on this analysis, integrating Ru-N2 and Ru-N4 into a single material is expected to create a synergistic effect between the two sites, leading to superior alkaline HER performance, potentially surpassing that of Pt/C.

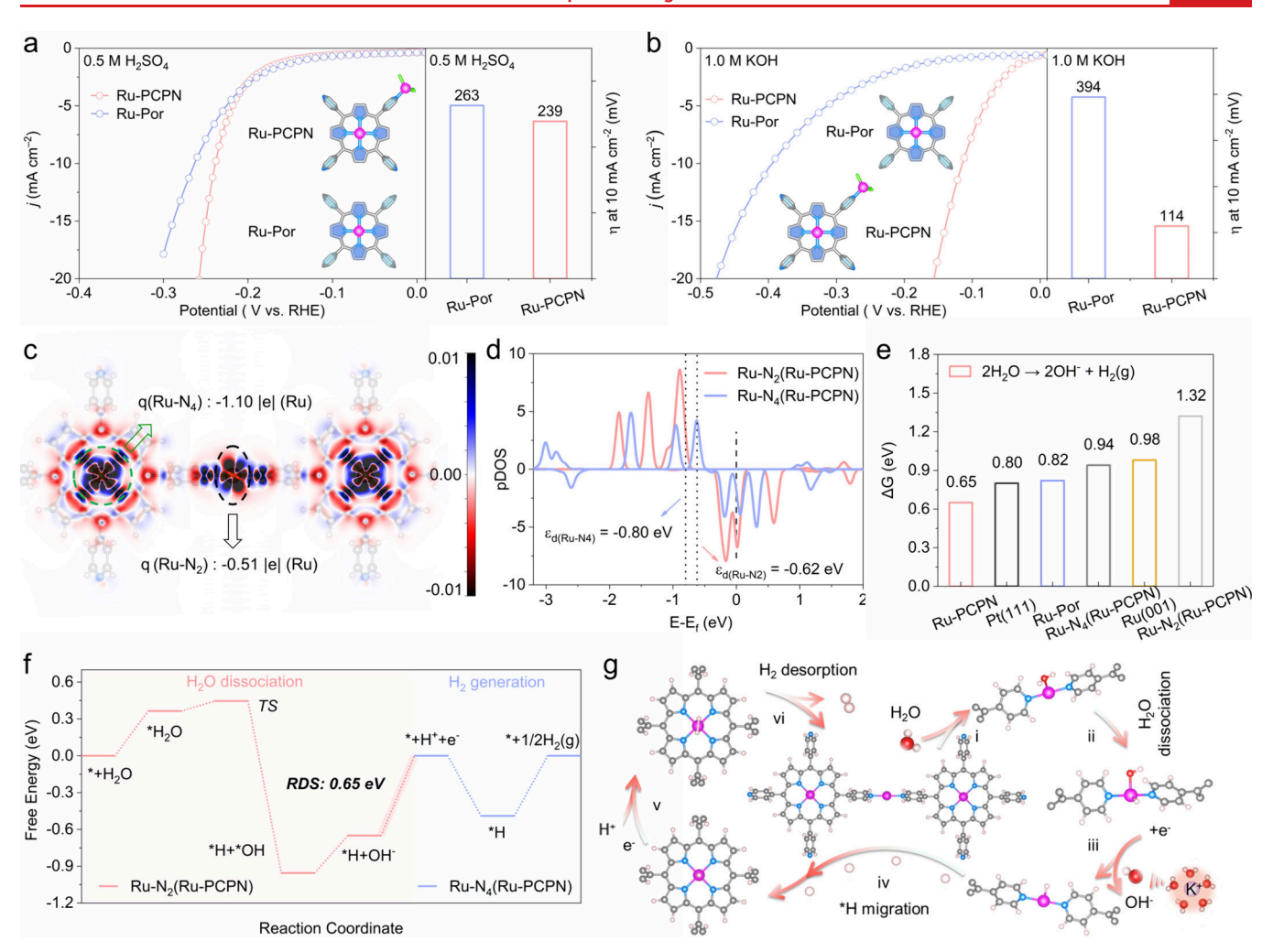


Figure 3. Mechanism analysis for the co-catalytic sites of Ru-PCPN. a) HER polarization curve of Ru-PCPN and Ru-Por in Ar-saturated 0.5 M H_2SO_4 and the overpotentials at 10 mA cm⁻². b) HER polarization curve of Ru-PCPN and Ru-Por in Ar-saturated 1.0 M KOH and the overpotentials at 10 mA cm⁻². c) Charge density difference and Bader analysis of Ru-PCPN. d) The calculated pDOS of Ru-PCPN. e) RDS energy barrier of the alkaline HER process $(2H_2O + 2e^- \rightarrow 2OH^- + H_2)$. f, g) Calculated free energy and reaction path diagram of the process of water dissociation to produce H_2 for Ru-PCPN (color code: orange, Ru; gray, C; blue, N; red, O; and white, H).

We then designed a bioinspired conjugated porphyrin coordination polymer network that simultaneously incorporated investigated Ru-N₄ and Ru-N₂ sites (Figure 2a). 48,49 Specifically, 5,10,15,20-tetra(4-pyridyl)-21H,23H-porphine (Tpyp) with typical planar conjugated structure and both pyridine-N and pyrrole-N were assembled with the Ru3+ to form the porphyrin coordination polymer networks with both Ru-N₄ and Ru-N₂ sites (Ru-PCPN), while the isolated Ru-N₄ catalytic sites (Ru-Por) were synthesized as control (Figure 2b and Figures S5, S6). 50 Fourier transform infrared spectra (FT-IR) observed the N-H absorption peaks of the Tpyp ligand at 3300 cm⁻¹ disappear in Ru-PCPN, indicating the formation of pyrrolic Ru-N sites in the porphyrin center (Figure 2c). 51 X-ray photoelectron spectroscopy (XPS) was further applied to gain insight into the electronic structure of Ru-PCPN and the elemental contents in the as-synthesized samples (Table S1). The high-resolution N 1s spectra of Ru-PCPN demonstrate obvious peak shifts of both pyridine N from 397.55 to 398.50 eV and pyrrolic N from 398.78 to 399.20 eV, thus demonstrating the formation of both Ru coordination (Figure 2d). Furthermore, both Ru-Por and Ru-PCPN show Ru 3p_{3/2} (from 462.08 to 461.97 eV) and Ru 3p_{1/2} (from 484.23 to 484.13 eV) assigned to ionic Ru,

confirming that all Ru atoms are coordinated to N and no metallic Ru is formed (Figure 2e). In addition, the structure of Ru-Por was confirmed by the presence of a single pyrrolic Ru-N coordination environment (Figure S7).

The intrinsic catalytic activity of Ru-PCPN toward HER has been explored in both alkaline (1.0 M KOH) and acidic (0.5 M H₂SO₄) solutions via the rotating disk electrode. The polarization curves display that the Ru-Por and Ru-PCPN exhibit similar overpotentials under acidic conditions (263 mV for Ru-Por and 239 mV for Ru-PCPN) to reach the current density of 10 mA cm⁻² (Figure 3a). However, when shifted to alkaline condition, the Ru-PCPN catalysts show muchenhanced activity with an overpotential of 114 mV and lower Tafel slope (90.4 mV dec⁻¹), much outperforming that of Ru-Por (394 mV and 258.1 mV dec⁻¹), which indicates that the additional $Ru-N_2$ sites in Ru-PCPN play a key role in alkaline conditions (Figure 3b and Figure S8). This key role can be attributed to the strong catalytic water dissociation ability of the Ru-N2 site and the synergistic effect between the Ru-N₄ and Ru-N₂ sites in Ru-PCPN. Then DFT calculations were performed to further elucidate the synergistic enhancement of the alkaline HER mechanism in Ru-PCPN by the Ru-N₄ and Ru-N₂ sites. As shown in Figure 3c, the charge density

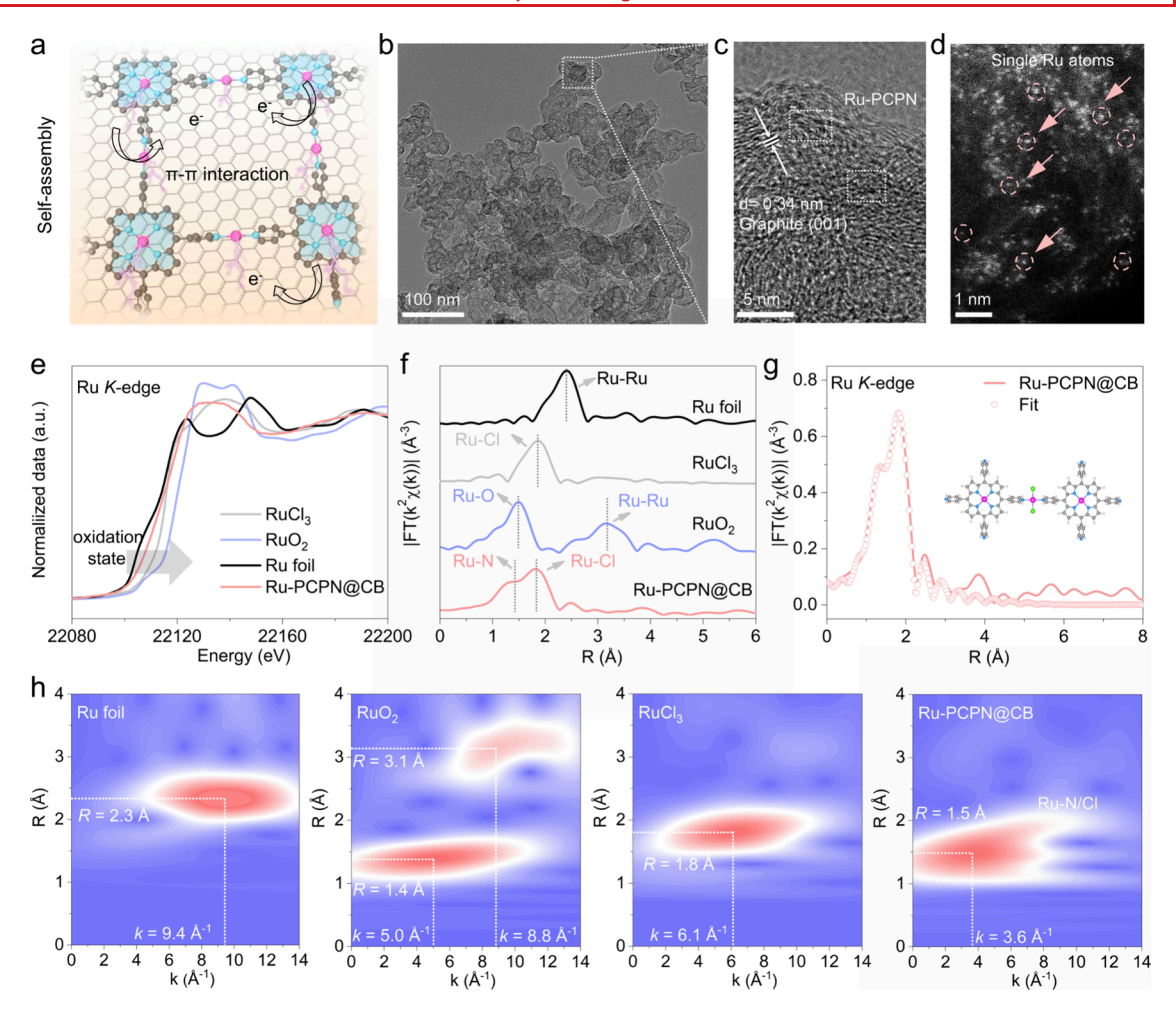


Figure 4. Morphology and detailed coordinated structure analysis of the Ru-PCPN@CB electrocatalysts. a) The synthetic diagram of Ru-PCPN self-assembly onto a carbon substrate. b) TEM and c) HR-TEM of Ru-PCPN@CB. d) HAADF-STEM of Ru-PCPN@CB (the bright dots corresponding to isolated Ru atoms). e) XANES spectra at the Ru K-edge. f) Ru k²-weighted FT-EXAFS for Ru foil, RuCl₃, RuO₂, and Ru-PCPN@CB. g) R-space EXAFS curve-fitting of Ru-PCPN@CB. h) Wavelet transformation of Ru K-edge EXAFS of Ru-PCPN@CB and references.

difference and Bader charge analyses indicate that the Ru- N_2 (Ru-PCPN) active center transfers fewer electrons (0.51 lel) to the adjacent N/C compared to Ru-N₄(Ru-PCPN) (1.10 | el), implying that the Ru-N₂(Ru-PCPN) site has a stronger metallic character and properties closer to Ru/C. The projected density of states (pDOS) of Ru-PCPN in Figure 3d shows that the $Ru-N_2(Ru-PCPN)$ site not only exhibits a higher d-band center (-0.62 eV) but also possesses more active electrons near the Fermi level than Ru-N₄(Ru-PCPN) (-0.80 eV). This suggests that Ru-N₂(Ru-PCPN) may have superior water dissociation capability and that different coordination environments can regulate the Ru-H binding energy to maximize HER activity. As shown in Figure S9, the individual performance of the Ru-N₂(Ru-PCPN) and Ru-N₄(Ru-PCPN) aligns with our expectations, with Ru-N₂(Ru-PCPN) exhibiting excellent water dissociation ability (RDS: 0.36 eV, comparable to Ru/C at 0.33 eV) and Ru-N₄(Ru-PCPN) demonstrating superior hydrogen recombination efficiency (RDS: 0.51 eV, superior to Pt/C at 0.67 eV).

In terms of the complete alkaline HER, neither the individual $Ru-N_4(Ru-PCPN)$ nor $Ru-N_2(Ru-PCPN)$ sites surpass Pt/C, with corresponding RDS values of 1.32, 0.94, and 0.8 eV, respectively (Figure 3e). Once there is a cocatalytic synergy between $Ru-N_2$ and $Ru-N_4$, the intrinsically alkaline HER activity of Ru-PCPN is greatly enhanced, and the

overall RDS is the removal of a H atom on Ru-N₂ (*H \rightarrow * + 1/2H₂), with an energy barrier of only 0.65 eV, which exceeds the performance of Pt/C (0.80 eV) (Figure 3f). As depicted in Figure 3g, the specific synergistic process of Ru-PCPN can be divided into (i-iii) the water-splitting process mediated by the Ru-N₂(Ru-PCPN) site; (iv) the migration of the generated *H from the Ru-N₂(Ru-PCPN) site to the Ru-N₄(Ru-PCPN) site through PCET (Figure S10); and (v, vi) hydrogen production process facilitated by the Ru-N₄(Ru-PCPN) site. The presence of the PCET process between the synergistic sites of Ru-N2 and Ru-N4 enables Ru-PCPN to gain a "hybrid advantage", thereby achieving superior alkaline HER activity compared to Pt/C, which was also demonstrated through in situ Raman spectra and in situ infrared spectra characterization (Figures S11, S12). In addition, the inferences about water dissociation and hydrogen recombination discussed in the first part still apply (Figures S13, S14).

For practical applications, Ru-PCPN can self-assemble onto the carbon substrate with the graphene-like surface in larger conjugated systems via $\pi-\pi$ intermolecular interactions to improve the conductivity and performance for electrocatalytic processes (Figure 4a). Different carbon substrates such as carbon black (CB), carbon nanotubes (CNTs), and reduced graphene oxide (rGO) are employed to load the Ru-PCPN catalysts with the weight ratio of 1:1, which are named Ru-

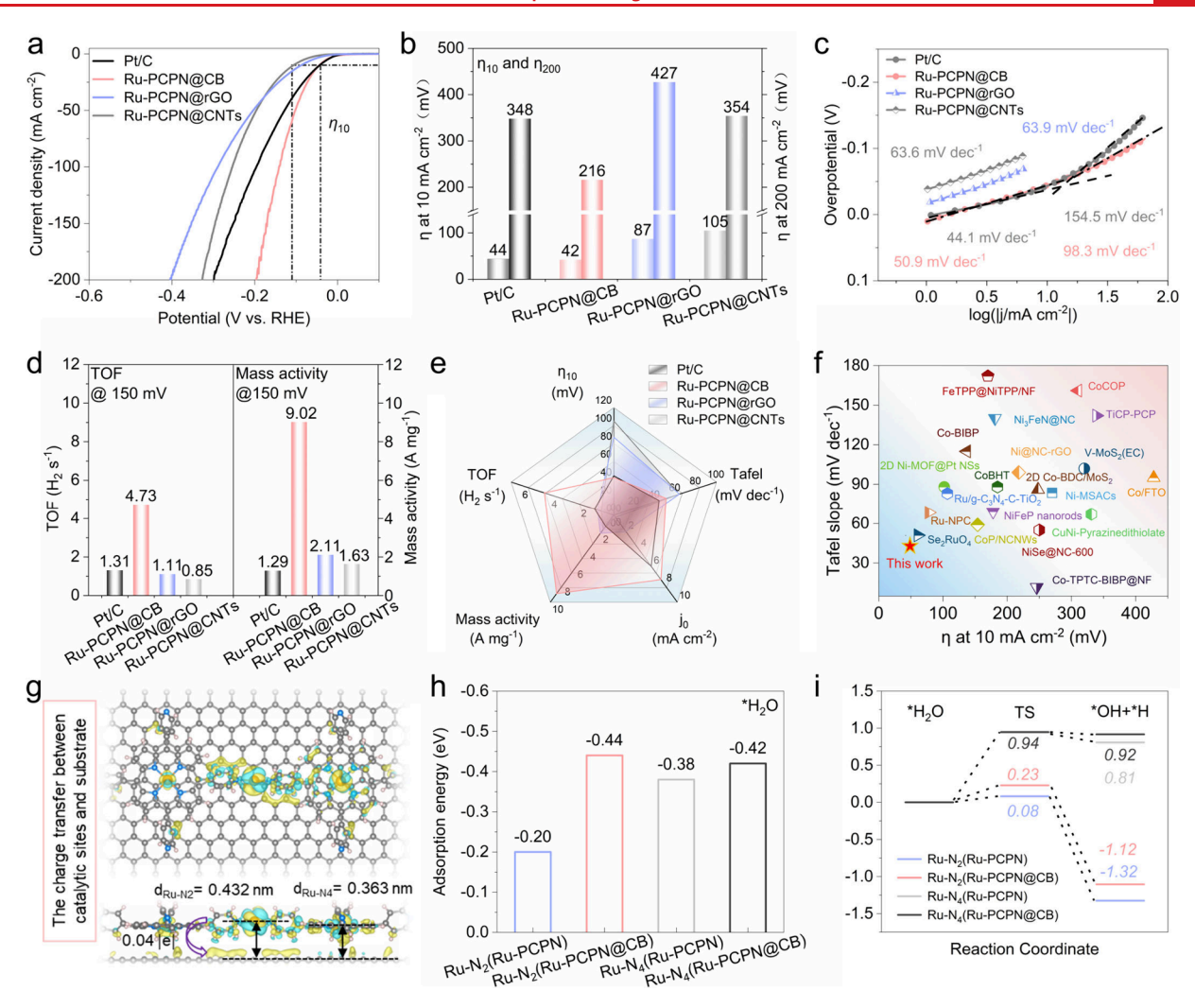


Figure 5. Electrocatalytic HER performance and theoretical investigations of the Ru-PCPN@CB electrocatalyst. a) HER polarization curves of different catalysts in 1 M KOH solution (scan rate: 10 mV s⁻¹; rotation speed: 1600 rpm). b) HER performance in 1 M KOH of different catalysts. c) Tafel plots. d) Comparison of the TOF and mass activity (the metal loading of the catalyst derives from the XPS results; ~12.9 μ g_{Ru} cm⁻², ~13.2 μ g_{Ru} cm⁻², and ~15.1 μ g_{Ru} cm⁻² for Ru-PCPN@CB, Ru-PCPN@rGO, and Ru-PCPN@CNTs; ~50 μ g_{Pt} cm⁻² for Pt/C). e) Comparison of the overall HER activity. f) Comparison of the overpotential of different catalysts at 10 mA cm⁻². g) The charge density difference and Bader analysis of Ru-PCPN@CB (cyan and yellow represent charge depletion and accumulation, respectively; the cutoff isosurface, 0.0005 e bohr⁻³). h) The adsorption energy of *H₂O. i) The calculated free energy diagram for water dissociation of Ru-PCPN and Ru-PCPN@CB.

PCPN@CB, Ru-PCPN@CNTs, and Ru-PCPN@rGO, respectively. Ultraviolet-visible (UV-vis) spectroscopy showed a red-shifted and broadened Soret band in carbon-modified Ru-PCPN compared to pristine Ru-PCPN, especially for Ru-PCPN@CB, indicative of superior interfacial $\pi - \pi$ coupling between Ru-PCPN and substrates (Figure S15). 53,54 Scanning electron microscopy (SEM) and transitional electron microscopy (TEM) images reveal that the supported Ru-PCPN catalysts exhibit typical nanoparticle, nanotube, and nanosheet structures of the substrates (Figure S16). High-resolution TEM images of the Ru-PCPN@CB, Ru-PCPN@CNTs, and Ru-PCPN@rGO reveal the distribution of the crystallized carbon substrate and amorphous Ru-PCPN, indicating the successful loading of Ru-PCPN on the substrates (Figure 4b,c and Figure S17). Then the atomic-resolution high-angle annular dark-field STEM (HAADF-STEM) analysis was performed on Ru-PCPN@CB as represented, where a crystallized carbon substrate and uniformly distributed Ru atoms are observed (Figure 4d).

To investigate the precise coordination structures and electronic states of Ru sites in Ru-PCPN@CB, X-ray absorption spectroscopy (XAS) measurements were conducted. As shown in Figure 4e, the X-ray absorption near edge structure (XANES) region shows that the Ru K-edge absorption edge position in Ru-PCPN@CB is between the RuCl₃ and Ru foil, indicating an oxidation state between Ru⁰ and Ru3+. The corresponding Fourier transform of the extended XAFS (FT-EXAFS) curve displays two main peaks at ~1.40 and 1.80 Å in the first shell, which can be assigned to Ru-N and Ru-Cl bonds, and no Ru-Ru peak is observed (Figure 4f). The EXAFS fitting analysis was also performed, indicating that the Ru-N sites are coordinated with Ru-N₂ via pyridine N and Ru-N₄ via pyrrole N (Figure 4g, Figures S18, S19, and Table S2). The wavelet transformation (WT) images give similar results on the Ru structure, where no Ru-Ru distribution is found (Figure 4h). Since Cl ions do not function as reactive sites but primarily stabilize the Ru-N2 configuration during material synthesis (forming Ru-N2Cl2, Figure S20) and are progressively removed or replaced by OH

intermediates during the electrocatalytic process (Figure S21), the discussion focuses exclusively on the Ru–N₂ configuration.

The electrochemical HER performances of those carbonsupported catalysts were evaluated in 1 M KOH electrolyte using a three-electrode system. As shown in Figures 5a and 5b, the optimized Ru-PCPN@CB delivers the lowest overpotential (42 and 216 mV), which outperforms the Pt/C (44 and 348 mV) at the current density of 10 and 200 mA cm⁻² in alkaline solution. Furthermore, compared to other carbon substrates, Ru-PCPN@CB (50.9 mV dec⁻¹) exhibits a Tafel slope similar to that of Pt/C (44.1 mV dec⁻¹), indicating its excellent kinetic activity and mixed Volmer-Heyrovsky mechanism (Figure 5c). Meanwhile, the highest exchange current density (j_0) of Ru-PCPN@CB (7.41 mA cm⁻²) also confirms the effective facilitation of the hydrogen generation kinetics (Figure S22). To assess the intrinsic activity of catalysts, the mass activity and turnover frequency (TOF) of catalysts were further calculated to reveal the activity per active site (Figure 5d and Figures S23-25). At an overpotential of 150 mV, Ru-PCPN@CB achieves a remarkable mass activity of 9.02 A mg⁻¹ and a TOF value of 4.73 s⁻¹, outperforming Ru-PCPN@CNTs (1.63 A mg^{-1} and 0.85 s⁻¹), Ru-PCPN@rGO (2.11 A mg^{-1} and 1.11 s^{-1}), and Pt/C (1.29 A mg⁻¹ and 1.31 s^{-1}). Compared with Ru-PCPN@rGO and Ru-PCPN@CNTs, Ru-PCPN@CB exhibits excellent electrochemical performance due to the enhanced interfacial synergy between CB and Ru-PCPN and accessibility of catalytic centers, which can be confirmed by electrochemical impedance spectroscopy (EIS) and electrochemical surface area (ECSA) analyses (Figures S26, S27). Based on the above analyses, an overall property evaluation indicates that Ru-PCPN@CB exhibits the lowest overpotential, the highest mass activity, TOF value, and j_0 , and a Tafel slope comparable to Pt/C, leading to the best catalytic performance (Figure 5e). Compared to recently reported representative HER electrocatalysts derived from annealing processes, the pyrolysis-free Ru-PCPN@CB catalysts with regularly arranged Ru-N coordination centers demonstrate superior HER performance (Figure 5f and Tables S3, S4). The stability of Ru-PCPN@CB to the continuous production of H2 was measured and compared with Pt/C. At a constant current density of 10 mA cm⁻², the overpotentials of Ru-PCPN@CB increased only slightly by 30 mV after running ~22 h, showcasing superior performance over Pt/C (Figure S28). Furthermore, the extended stability evaluations of Ru-PCPN@ CB under 20, 50, and 100 mA cm⁻² demonstrated a slight overpotential increase (17, 11, and 7 mV over 24 h, respectively, Figure S29), negligible Ru dissolution ratio (0.54%, Figure S30), and preserved Ru atomic dispersion (HAADF-STEM, Figure S31), confirming its good stability. The enhanced activity can be attributed to the synergistic interaction between Ru−N₂ and Ru−N₄ in Ru-PCPN, coupled with the highly conductive carbon substrate, which provides abundant active sites and facilitates rapid intermolecular charge and mass transport.

Based on experimental characterization, we initially discuss the impact of the carbon substrate on the catalytic performance of the material and construct two models: Ru-PCPN and Ru-PCPN@CB (Figure S32). As illustrated in Figure 5g and Figure S33, the interlayer exchange of electrons is limited to approximately 0.04 lel due to the steric hindrance of the benzene rings, thereby preventing overstacking that would hinder the effective exposure of active sites. Figure S34 further indicates that the presence of graphene has a minimal effect on

the adsorption and recombination processes of hydrogen. Interestingly, the presence of a carbon substrate significantly influences its ability to capture *H₂O (Figure 5h,i), particularly at the Ru–N₂ sites, thereby reducing the water dissociation RDS energy barrier from 0.36 eV (Ru–N₂(Ru-PCPN), * + H₂O \rightarrow *H₂O) to 0.23 eV (Ru–N₂(Ru-PCPN@CB), *H₂O \rightarrow *OH + *H). These results suggest that the presence of the carbon substrate can further enhance the water dissociation performance and thus increase the alkaline HER activity.

In summary, inspired by the co-catalytic architectures of metalloenzymes, we have successfully engineered adjacent Ru-N₂ and Ru-N₄ sites at molecular precision to replicate nature's proton-electron coupling efficiency. Systematic DFT analysis reveals a stepwise catalytic mechanism: the electronrich Ru-N₂ site lowers the water dissociation barrier, while the neighboring Ru-N₄ center optimizes hydrogen recombination through directed proton migration via the PCET pathway. This dual active site synergistic effect completely avoids the rate-limiting Volmer step (H-OH bond cleavage), reducing the overall hydrogen evolution energy barrier. Experimental validation demonstrates that the Ru-PCPN@CB catalyst achieves benchmark alkaline HER performance surpassing that of the Pt/C catalyst. Our work crystallizes two fundamental design principles: 1) atomic-scale proximity of functionally complementary sites enables parallel reaction coordinate optimization; 2) directional PCET pathways can circumvent traditional adsorption-energy scaling relationships. This biomimetic coordination strategy shows generic potential for multistep catalytic reactions requiring spatially resolved active centers.

ASSOCIATED CONTENT

Supporting Information

The Supporting Information is available free of charge at https://pubs.acs.org/doi/10.1021/acs.nanolett.5c01504.

Experimental details, materials, and methods; supplemental TEM, SEM, XPS, ICP-MS, UV-vis, in situ infrared spectra, and in situ Raman spectra; XAS fitting spectra and parameters; DFT analysis of electronic structure and reaction mechanism; electrochemical analysis (PDF)

AUTHOR INFORMATION

Corresponding Authors

Tian Ma — College of Polymer Science and Engineering, National Key Laboratory of Advanced Polymer Materials, Sichuan University, Chengdu 610065, China; ⊚ orcid.org/ 0000-0003-2062-4884; Email: matian1991@scu.edu.cn

Shuang Li — College of Polymer Science and Engineering, National Key Laboratory of Advanced Polymer Materials, Sichuan University, Chengdu 610065, China; ⊚ orcid.org/ 0000-0001-7414-630X; Email: shuang.li@scu.edu.cn

Authors

Zhenyang Zhao — College of Polymer Science and Engineering, National Key Laboratory of Advanced Polymer Materials, Sichuan University, Chengdu 61006S, China; orcid.org/ 0000-0001-8535-0357

Chao He − College of Polymer Science and Engineering, National Key Laboratory of Advanced Polymer Materials, Sichuan University, Chengdu 61006S, China; orcid.org/ 0000-0002-3259-3176

- Luchang Liu College of Polymer Science and Engineering, National Key Laboratory of Advanced Polymer Materials, Sichuan University, Chengdu 610065, China
- Yijuan Zheng College of Polymer Science and Engineering, National Key Laboratory of Advanced Polymer Materials, Sichuan University, Chengdu 61006S, China; orcid.org/ 0000-0003-0685-9812
- Wenhui Xiang College of Polymer Science and Engineering, National Key Laboratory of Advanced Polymer Materials, Sichuan University, Chengdu 610065, China
- Qinlong Wen Department of Biotherapy, Cancer Center, West China Hospital, Sichuan University, Chengdu 610041, China
- Yinghan Wang College of Polymer Science and Engineering, National Key Laboratory of Advanced Polymer Materials, Sichuan University, Chengdu 610065, China; ◎ orcid.org/ 0000-0001-7002-3097
- Evgeniya Sheremet Tomsk Polytechnic University, Tomsk 634050, Russia

Complete contact information is available at: https://pubs.acs.org/10.1021/acs.nanolett.5c01504

Author Contributions

Z.Z. and T.M. performed the experiments and analyzed the results. C.H., L.L., J.Z., W.X., Q.W., and Y.W. assisted with the figure production, experiment design, and data acquisition. S.L. and Z.Z. designed and conducted the theoretical calculation. Z.Z., E.S., T.M., and S.L. wrote and edited the manuscript. Z.Z. and S.L. conceived the idea and designed the experiments. L.S. supervised the whole project. All authors discussed the results and commented on the manuscript.

Notes

The authors declare no competing financial interest.

ACKNOWLEDGMENTS

This work was financially supported by the National Natural Science Foundation of China (Nos. 52273269, 52203177, 52473278, and 52473136), Sichuan Science and Technology Program (2024YFHZ0041, 2025YFHZ0188, 2025YFHZ0192), and the Fundamental Research Funds for the Central Universities. We thank our laboratory members for their generous help and gratefully acknowledge the help of Dr. Mi Zhou at Sichuan University. We also appreciate the Analytical & Testing Center of Sichuan University.

REFERENCES

- (1) Zhang, B.; Zheng, Y.; Ma, T.; Yang, C.; Peng, Y.; Zhou, Z.; Zhou, M.; Li, S.; Wang, Y.; Cheng, C. Designing MOF Nanoarchitectures for Electrochemical Water Splitting. *Adv. Mater.* **2021**, 33, 2006042.
- (2) Cao, X.; Wang, T.; Jiao, L. Transition-Metal (Fe, Co, and Ni)-Based Nanofiber Electrocatalysts for Water Splitting. *Adv. Fiber Mater.* **2021**, 3 (4), 210–228.
- (3) Zhang, Y.; Yan, R.; Xu, X.; He, C.; Zhou, M.; Zeng, Z.; Ma, T.; Wang, M.; Li, S. Next Generation Noble Metal-Engineered Catalysts: From Structure Evolution to Structure-Reactivity Correlation in Water Splitting. *Adv. Funct. Mater.* **2024**, *34* (4), 2308813.
- (4) Yang, H.; Ji, Y.; Shao, Q.; Zhu, W.; Fang, M.; Ma, M.; Liao, F.; Huang, H.; Zhang, Y.; Yang, J.; Fan, Z.; Li, Y.; Liu, Y.; Shao, M.; Kang, Z. Metastable-phase platinum oxide for clarifying the Pt-O active site for the hydrogen evolution reaction. *Energy Environ. Sci.* **2023**, *16* (2), 574–583.
- (5) Fan, L. H.; Deng, H.; Zhang, Y. G.; Du, Q.; Leung, D. Y. C.; Wang, Y.; Jiao, K. Towards ultralow platinum loading proton

- exchange membrane fuel cells. Energy Environ. Sci. 2023, 16 (4), 1466–1479.
- (6) Ma, T.; Cao, H.; Li, S.; Cao, S.; Zhao, Z.; Wu, Z.; Yan, R.; Yang, C.; Wang, Y.; van Aken, P. A.; Qiu, L.; Wang, Y.-G.; Cheng, C. Crystalline Lattice-Confined Atomic Pt in Metal Carbides to Match Electronic Structures and Hydrogen Evolution Behaviors of Platinum. *Adv. Mater.* 2022, 34 (41), 2206368.
- (7) Tan, H.; Tang, B.; Lu, Y.; Ji, Q.; Lv, L.; Duan, H.; Li, N.; Wang, Y.; Feng, S.; Li, Z.; Wang, C.; Hu, F.; Sun, Z.; Yan, W. Engineering a local acid-like environment in alkaline medium for efficient hydrogen evolution reaction. *Nat. Commun.* **2022**, *13* (1), 2024.
- (8) Zheng, Y.; Geng, W.; Xiao, S.; Ma, T.; Cheng, C.; Liao, Y.; Zeng, Z.; Li, S.; Zhao, C. Interfacial Ir-V Direct Metal Bonding Enhanced Hydrogen Evolution Activity in Vanadium Oxides Supported Catalysts. *Angew. Chem. Int. Ed.* **2024**, *63* (35), No. e202406427.
- (9) Chen, X.; Wang, X.-T.; Le, J.-B.; Li, S.-M.; Wang, X.; Zhang, Y.-J.; Radjenovic, P.; Zhao, Y.; Wang, Y.-H.; Lin, X.-M.; Dong, J.-C.; Li, J.-F. Revealing the role of interfacial water and key intermediates at ruthenium surfaces in the alkaline hydrogen evolution reaction. *Nat. Commun.* 2023, 14 (1), 5289.
- (10) Wu, Z.; Liu, L.; Zhao, Z.; Yang, C.; Mu, S.; Zhou, H.; Luo, X.; Ma, T.; Li, S.; Zhao, C. Modulating Electronic Environment of Ru Nanoclusters via Local Charge Transfer for Accelerating Alkaline Water Electrolysis. *Small* **2023**, *19* (2), 2204738.
- (11) Wang, K.; Zhou, J.; Sun, M.; Lin, F.; Huang, B.; Lv, F.; Zeng, L.; Zhang, Q.; Gu, L.; Luo, M.; Guo, S. Cu-Doped Heterointerfaced Ru/RuSe2 Nanosheets with Optimized H and H2O Adsorption Boost Hydrogen Evolution Catalysis. *Adv. Mater.* **2023**, *35* (23), 2300980.
- (12) Jung, K.; Pratama, D. S. A.; Haryanto, A.; Jang, J. I.; Kim, H. M.; Kim, J.-C.; Lee, C. W.; Kim, D.-W. Iridium-Cluster-Implanted Ruthenium Phosphide Electrocatalyst for Hydrogen Evolution Reaction. *Adv. Fiber Mater.* **2024**, *6* (1), 158–169.
- (13) Liu, Q.; Lu, B.; Nichols, F.; Ko, J.; Mercado, R.; Bridges, F.; Chen, S. Rapid preparation of carbon-supported ruthenium nanoparticles by magnetic induction heating for efficient hydrogen evolution reaction in both acidic and alkaline media. *SusMat* **2022**, 2 (3), 335–346.
- (14) Wang, L.; Tao, H.; Liu, Y.; Chen, Y.; Chen, Z.; Yang, X.; Yang, B.; Li, Z.; Dai, Q.; Lian, C.; Lei, L.; Hou, Y. Multiscale modulation of ultra-small ruthenium anchored on bimetallic sulfides for seawater electrolysis at ampere-level current density. *Nano Energy* **2024**, *124*, 109481.
- (15) Qiu, Y.; Rao, Y.; Zheng, Y.; Hu, H.; Zhang, W.; Guo, X. Activating ruthenium dioxide via compressive strain achieving efficient multifunctional electrocatalysis for Zn-air batteries and overall water splitting. *InfoMat* **2022**, *4* (9), No. e12326.
- (16) Yao, Q.; Huang, B.; Zhang, N.; Sun, M.; Shao, Q.; Huang, X. Channel-Rich RuCu Nanosheets for pH-Universal Overall Water Splitting Electrocatalysis. *Angew. Chem. Int. Ed.* **2019**, *58* (39), 13983–13988.
- (17) Yang, Y.; Kim, J.; Kim, C.; Seong, A.; Kwon, O.; Lee, J. H.; Kristanto, I.; Zhang, L.; Zhou, J.; Wang, J.-Q.; Baek, J.-B.; Kwak, S. K.; Kim, G. Edge-selective decoration with ruthenium at graphitic nanoplatelets for efficient hydrogen production at universal pH. *Nano Energy* **2020**, *76*, 105114.
- (18) Kweon, D. H.; Okyay, M. S.; Kim, S.-J.; Jeon, J.-P.; Noh, H.-J.; Park, N.; Mahmood, J.; Baek, J.-B. Ruthenium anchored on carbon nanotube electrocatalyst for hydrogen production with enhanced Faradaic efficiency. *Nat. Commun.* **2020**, *11* (1), 1278.
- (19) Yang, C.; Wu, Z.; Zheng, Y.; Gao, Y.; Ma, T.; Zeng, Z.; Wang, Y.; Cheng, C.; Li, S. Electron-Donating Cu Atoms Induced High Proton Supply and Anti-Poisoning Ruthenium Clusters for Superior Direct Seawater Hydrogen Production. *Adv. Funct. Mater.* **2024**, *34* (40), 2404061.
- (20) Zhang, Y.; Zheng, W.; Wu, H.; Zhu, R.; Wang, Y.; Wang, M.; Ma, T.; Cheng, C.; Zeng, Z.; Li, S. Tungsten oxide-anchored Ru clusters with electron-rich and anti-corrosive microenvironments for efficient and robust seawater splitting. SusMat 2024, 4 (1), 106–115.

- (21) Wu, H.; Zhao, Z.; Wang, M.; Zheng, W.; Zhang, Y.; Wang, Y.; Ma, T.; Zeng, Z.; Cheng, C.; Li, S. Alkaline-earth-metal regulated metal carbides with bioinspired gradient OH spillover for efficient and long-lasting direct seawater electrolysis. *J. Mater. Chem. A* **2024**, *12* (18), 10755–10763.
- (22) Yang, C.; Wu, Z.; Zhao, Z.; Gao, Y.; Ma, T.; Luo, X.; Cheng, C.; Wang, Y.; Li, S.; Zhao, C. Mn-Oxygen Compounds Coordinated Ruthenium Sites with Deprotonated and Low Oxophilic Microenvironments for Membrane Electrolyzer-Based H2-Production. *Adv. Mater.* **2023**, 35 (38), 2303331.
- (23) Wang, K.; Cao, J.; Yang, X.; Sang, X.; Yao, S.; Xiang, R.; Yang, B.; Li, Z.; O'Carroll, T.; Zhang, Q.; Lei, L.; Wu, G.; Hou, Y. Kinetically Accelerating Elementary Steps via Bridged Ru-H State for the Hydrogen-Evolution in Anion-Exchange Membrane Electrolyzer. *Adv. Funct. Mater.* **2023**, 33 (16), 2212321.
- (24) Yang, Y.; Yu, Y.; Li, J.; Chen, Q.; Du, Y.; Rao, P.; Li, R.; Jia, C.; Kang, Z.; Deng, P.; Shen, Y.; Tian, X. Engineering Ruthenium-Based Electrocatalysts for Effective Hydrogen Evolution Reaction. *Nano Micro Lett.* **2021**, *13* (1), 160.
- (25) Li, L.; Tian, F.; Qiu, L.; Wu, F.; Yang, W.; Yu, Y. Recent Progress on Ruthenium-Based Electrocatalysts towards the Hydrogen Evolution Reaction. *Catalysts* **2023**, *13* (12), 1497.
- (26) Kim, M.; Kim, S.-h.; Park, J.; Lee, S.; Jang, I.; Kim, S.; Lee, C. Y.; Kwon, O. J.; Ham, H. C.; Hupp, J. T.; Jung, N.; Yoo, S. J.; Whang, D. Reconstructing Oxygen-Deficient Zirconia with Ruthenium Catalyst on Atomic-Scale Interfaces toward Hydrogen Production. *Adv. Funct. Mater.* **2023**, 33 (29), 2300673.
- (27) Chen, J.; Huang, J.; Wang, R.; Feng, W.; Wang, H.; Luo, T.; Hu, Y.; Yuan, C.; Feng, L.; Cao, L.; Kajiyoshi, K.; He, C.; Liu, Y.; Li, Z.; Feng, Y. Atomic ruthenium coordinated with chlorine and nitrogen as efficient and multifunctional electrocatalyst for overall water splitting and rechargeable zinc-air battery. *Chem. Eng. J.* **2022**, 441. 136078.
- (28) Liu, T.; Pu, Z.; Chen, Z.; Wu, M.; Xia, Y.; Liu, S.; Chen, N.; Chen, W.; Zhang, L.; Chen, Z.; Zhang, G.; Sun, S. In situ electrochemical synthesis of atomically dispersed metal sites for efficient hydrogen evolution reaction. *SusMat* **2024**, *4* (6), No. e246.
- (29) Zheng, Y.; Xiao, S.; Xing, Z.; Wu, H.; Ma, T.; Zeng, Z.; Liao, Y.; Li, S.; Cheng, C.; Zhao, C. Oxophilic vanadium and deprotonated ruthenium atoms on tungsten carbide with accelerated intermediate migration for high-performance seawater hydrogen evolution. *Nano Energy* **2024**, *127*, 109769.
- (30) Lu, B.; Guo, L.; Wu, F.; Peng, Y.; Lu, J. E.; Smart, T. J.; Wang, N.; Finfrock, Y. Z.; Morris, D.; Zhang, P.; Li, N.; Gao, P.; Ping, Y.; Chen, S. Ruthenium atomically dispersed in carbon outperforms platinum toward hydrogen evolution in alkaline media. *Nat. Commun.* **2019**, *10* (1), 631.
- (31) Kou, Z.; Liu, Y.; Cui, W.; Yang, B.; Li, Z.; Rodriguez, R. D.; Zhang, Q.; Dong, C.-L.; Sang, X.; Lei, L.; Zhang, T.; Hou, Y. Electronic structure optimization of metal-phthalocyanine via confining atomic Ru for all-pH hydrogen evolution. *Energy Environ. Sci.* 2024, 17 (4), 1540–1548.
- (32) Wu, C.; Ding, S.; Liu, D.; Li, D.; Chen, S.; Wang, H.; Qi, Z.; Ge, B.; Song, L. A Unique Ru-N4-P Coordinated Structure Synergistically Waking Up the Nonmetal P Active Site for Hydrogen Production. *Research* **2020**, 2020, 5860712.
- (33) Zhang, H.; Zhou, W.; Lu, X. F.; Chen, T.; Lou, X. W. Implanting Isolated Ru Atoms into Edge-Rich Carbon Matrix for Efficient Electrocatalytic Hydrogen Evolution. *Adv. Energy Mater.* **2020**, *10* (23), 2000882.
- (34) Chao, T.; Xie, W.; Hu, Y.; Yu, G.; Zhao, T.; Chen, C.; Zhang, Z.; Hong, X.; Jin, H.; Wang, D.; Chen, W.; Li, X.; Hu, P.; Li, Y. Reversible hydrogen spillover at the atomic interface for efficient alkaline hydrogen evolution. *Energy Environ. Sci.* **2024**, *17* (4), 1397–1406.
- (35) Yang, J.; Yang, S.; An, L.; Zhu, J.; Xiao, J.; Zhao, X.; Wang, D. Strain-Engineered Ru-NiCr LDH Nanosheets Boosting Alkaline Hydrogen Evolution Reaction. ACS Catal. 2024, 14 (5), 3466–3474.

- (36) Mu, X.; Zhang, X.; Chen, Z.; Gao, Y.; Yu, M.; Chen, D.; Pan, H.; Liu, S.; Wang, D.; Mu, S. Constructing Symmetry-Mismatched RuxFe3-xO4 Heterointerface-Supported Ru Clusters for Efficient Hydrogen Evolution and Oxidation Reactions. *Nano Lett.* **2024**, *24* (3), 1015–1023.
- (37) Sun, Y.; Xue, Z.; Liu, Q.; Jia, Y.; Li, Y.; Liu, K.; Lin, Y.; Liu, M.; Li, G.; Su, C.-Y. Modulating electronic structure of metal-organic frameworks by introducing atomically dispersed Ru for efficient hydrogen evolution. *Nat. Commun.* **2021**, *12* (1), 1369.
- (38) Hammes-Schiffer, S. Proton-Coupled Electron Transfer: Moving Together and Charging Forward. J. Am. Chem. Soc. 2015, 137 (28), 8860–8871.
- (39) Tyburski, R.; Liu, T.; Glover, S. D.; Hammarström, L. Proton-Coupled Electron Transfer Guidelines, Fair and Square. *J. Am. Chem. Soc.* **2021**, *143* (2), 560–576.
- (40) Hutchison, P.; Soudackov, A. V.; Hammes-Schiffer, S. Nonadiabatic Proton-Coupled Electron Transfer at a Graphitic Surface Immobilized Cobalt Porphyrin. *ACS Catal.* **2024**, *14* (19), 14363–14372.
- (41) Das, P.; Ball, B.; Sarkar, P. Bifunctional Electrocatalytic Activity of Two-Dimensional Metallophthalocyanine-Based Metal-Organic-Frameworks for Overall Water Splitting: A DFT Study. *ACS Catal.* **2023**, *13* (24), 16307–16317.
- (42) Wang, Z.; Feng, S.; Rovira, C.; Wang, B. How Oxygen Binding Enhances Long-Range Electron Transfer: Lessons From Reduction of Lytic Polysaccharide Monooxygenases by Cellobiose Dehydrogenase. *Angew. Chem. Int. Ed.* **2021**, *60* (5), 2385–2392.
- (43) Yu, S.; Yamauchi, H.; Wang, S.; Aggarwal, A.; Kim, J.; Gordiz, K.; Huang, B.; Xu, H.; Zheng, D. J.; Wang, X.; Iriawan, H.; Menga, D.; Shao-Horn, Y. CO2-to-methanol electroconversion on a molecular cobalt catalyst facilitated by acidic cations. *Nat. Catal.* **2024**, *7* (9), 1000–1009.
- (44) Li, J.; Huang, H.; Xue, W.; Sun, K.; Song, X.; Wu, C.; Nie, L.; Li, Y.; Liu, C.; Pan, Y.; Jiang, H.-L.; Mei, D.; Zhong, C. Self-adaptive dual-metal-site pairs in metal-organic frameworks for selective CO2 photoreduction to CH4. *Nat. Catal.* **2021**, *4* (8), 719–729.
- (45) Chakrabarti, S.; Sinha, S.; Tran, G. N.; Na, H.; Mirica, L. M. Characterization of paramagnetic states in an organometallic nickel hydrogen evolution electrocatalyst. *Nat. Commun.* **2023**, *14* (1), 905.
- (46) Shao, W.; Xing, Z.; Xu, X.; Ye, D.; Yan, R.; Ma, T.; Wang, Y.; Zeng, Z.; Yin, B.; Cheng, C.; Li, S. Bioinspired Proton Pump on Ferroelectric HfO2-Coupled Ir Catalysts with Bidirectional Hydrogen Spillover for pH-Universal and Superior Hydrogen Production. *J. Am. Chem. Soc.* **2024**, *146* (40), 27486–27498.
- (47) Wang, T.; Guo, L.; Jiang, Z.; Chen, S.; Xu, S.; Zhang, Y.; Zhang, J.; Li, R.; Peng, T. Ru-Pincer Complex-Bridged Cu-Porphyrin Polymer for Robust (Photo)Electrocatalytic H2 Evolution via Single-Atom Active Sites. *Adv. Funct. Mater.* **2021**, *31* (50), 2107290.
- (48) Ortega-Guerrero, A.; Fumanal, M.; Capano, G.; Tavernelli, I.; Smit, B. Insights into the Electronic Properties and Charge Transfer Mechanism of a Porphyrin Ruthenium-Based Metal-Organic Framework. *Chem. Mater.* **2020**, 32 (10), 4194–4204.
- (49) Lan, G.; Zhu, Y.-Y.; Veroneau, S. S.; Xu, Z.; Micheroni, D.; Lin, W. Electron Injection from Photoexcited Metal-Organic Framework Ligands to Ru2 Secondary Building Units for Visible-Light-Driven Hydrogen Evolution. *J. Am. Chem. Soc.* **2018**, *140* (16), 5326–5329.
- (50) Li, Q.; Zhao, Z.; Wang, T.; Adeli, M.; Xu, X.; Luo, X.; Cheng, C. Upgrading the Bioinspired Iron-Polyporphyrin Structures by Abiological Metals Toward New-Generation Reactive Oxygen Biocatalysts. *Nano Lett.* **2025**, 25 (4), 1404–1413.
- (51) Guo, J.; Xing, Z.; Liu, L.; Sun, Y.; Zhou, H.; Bai, M.; Liu, X.; Adeli, M.; Cheng, C.; Han, X. Antioxidase-Like Nanobiocatalysts with Ultrafast and Reversible Redox-Centers to Secure Stem Cells and Periodontal Tissues. *Adv. Funct. Mater.* **2023**, *33* (15), 2211778.
- (52) Cao, S.; Zhao, Z.; Zheng, Y.; Wu, Z.; Ma, T.; Zhu, B.; Yang, C.; Xiang, X.; Ma, L.; Han, X.; Wang, Y.; Guo, Q.; Qiu, L.; Cheng, C. A Library of ROS-Catalytic Metalloenzyme Mimics with Atomic Metal Centers. *Adv. Mater.* **2022**, *34* (16), No. e2200255.

(53) Yu, J.; Mathew, S.; Flavel, B. S.; Johnston, M. R.; Shapter, J. G. Ruthenium Porphyrin Functionalized Single-Walled Carbon Nanotube Arrays—A Step Toward Light Harvesting Antenna and Multibit Information Storage. *J. Am. Chem. Soc.* 2008, 130 (27), 8788–8796. (54) Wu, L.; Wang, J.; Feng, L.; Ren, J.; Wei, W.; Qu, X. Label-Free Ultrasensitive Detection of Human Telomerase Activity Using Porphyrin-Functionalized Graphene and Electrochemiluminescence Technique. *Adv. Mater.* 2012, 24 (18), 2447–2452.